Phaseless Multistatic Synthetic Aperture Radar Imaging

Bariscan Yonel , *Member, IEEE*, Nazia Choudhury , *Graduate Student Member, IEEE*, and Birsen Yazici , *Fellow, IEEE*

Abstract—**Multistatic phaseless synthetic aperture radar (SAR) is a novel imaging modality that offers advantages in reduced hardware complexity, operability at high frequencies, robustness, jamming resistance, and improved accuracy and resolution. Illumination diversity is a key facilitator in designing novel phaseless imaging systems for applications in optics, and with growing interest in radio-frequency sensing. In this article, we present a novel multistatic phaseless SAR imaging method using stochastic waveforms and the nonconvex Wirtinger flow (WF) framework that provides performance guarantees under sufficient conditions known to hold for certain random forward models. We present multiple variations of the WF algorithm including different initialization and regularization methods and study the tradeoffs between the performance of our algorithms with respect to the resources needed for phaseless multistatic imaging. Our extensive numerical simulations show that the waveform-diverse random illumination approach coupled with optimization-based reconstruction provides near-exact imaging with a limited number of transmitters and a single receiver, promoting our method for practical realization of phaseless multistatic SAR.**

Index Terms—**Multi-static synthetic aperture radar, phaseless radar, phase retrieval, Wirtinger flow.**

I. Introduction

PHASELESS synthetic aperture radar (SAR) is a novel, waveform-diverse imaging approach, which may have profound implications in system design, cost, and robustness for remote sensing applications. In this article, we present a novel multistatic phaseless SAR imaging method using stochastic waveforms and nonconvex phase retrieval algorithms with performance guarantees.

A. Motivations for Phaseless SAR

Phaseless SAR is not only a novel modality but also offers several advantages over conventional coherent SAR. The quality of conventional SAR imagery depends on the accurate phase information, which is often susceptible to errors arising from nonidealized acquisition conditions such as random motion of antennas [1] or perturbations in the propagation medium [2].

Such phase errors lead to significant degradation in image reconstruction [3], [4]. The sources of these errors, on the other hand, do not affect the amplitude of backscattered signals [5], promoting phaseless imaging as a desirable approach in dealing with the uncertainties in antenna location or signal trajectory [6]. In coherent sensing at high frequencies, the phase of the received signals is often too corrupted to meet the accuracy requirements of imaging [7], [8]. Difficulties directly arise due to the interaction between the probes, the noise in the phase demodulator in the receiver, and temperature drifts in the circuitry [8]. Accurate recording of phases can, therefore, be challenging above 10 GHz [4], [9], [10]. Phaseless SAR offers the capabilities to operate at high frequencies. Thus, synthetic aperture imaging at high-frequency bands calls for the development of novel computational methods that are capable of recovering targets from phaseless measurements. Furthermore, recording intensity-only measurements requires less expensive hardware with lower complexity on the RF back-end of antenna systems compared to coherent sensing [9], [11], [12]. Additionally, stochastic waveforms have the advantage of a low probability of intercept due to the agility of their parameters [13], [14]. Consequently, phaseless SAR imaging contributes toward the practical realization of multistatic SAR systems that can be deployed on a large number of small, unmanned aerial vehicles (UAVs) with benefits in robustness, cost, jamming resistance, improved accuracy and resolution [15], [16], and the ability to operate in contested environments [17], [18], [19].

B. Related Work

The aforementioned motivations have propelled the continued interest and research on phaseless wave-based imaging and remote sensing. To this end, the uniqueness of the inverse scattering problem from phaseless far-field patterns with known support and smooth boundary conditions has been studied and established in [20], [21], [22], [23], and [24]. Xu et al. [25] have shown that the scattered field intensities obtained in the far-field due to superposed pairs of plane wave incident fields uniquely determine the unknown reflectivity when there is full spatial diversity in receive and transmit. In imaging applications with antenna arrays, image reconstruction methods using intensity-only data have been developed using illumination protocols, which are designed to invoke the polarization identity [10], [26]. These techniques use pairwise simultaneous illuminations emitted from the array elements and are capable of recovering

the phase of M distinct measurements, if $3M - 2$ illuminations are used [6]. After phase recovery, the image reconstruction is performed using classical time-reversal methods [10], [26] or the MUSIC algorithm for recovering pointlike scatterers [27], [28]. In [6], the illumination protocol is extended to the setting of synthetic aperture imaging. However, the protocol requires sequential illumination for each fast-time frequency per location in the synthetic aperture, thus lengthening the acquisition process and limiting the applicability of the method to airborne SAR.

More recently, optimization-based phase retrieval theory has been studied and established for *random forward models* that are realized from Gaussian distribution [29], [30], or coded diffraction patterns for optical imaging using random modulating masks [31], [32], [33]. While theoretically important, these methods have been limited in their applicability to inverse problems in radar and wave-based imaging [9], [34], [35], [36], [37], [38] due to the mismatch between their assumptions and the deterministic nature of forward models in conventional imaging configurations [39], [40].

In [41], [42], [43], and [44], radar coincidence imaging (RCI) has been developed as an alternative imaging technique for RF sensing applications. These methods utilize multitransmitter configurations that emit stochastic waveforms to enable illuminations that approximate Gaussian statistics as the number of transmitters increases. The foundations of RCI are based on the computational ghost imaging modality [45], [46], [47], where an optical image is reconstructed using a bucket detector and a single continuous-wave laser pulse that is spatially incoherent. While the applicability of the principles of ghost imaging is well studied for radar with phase information, its phaseless counterpart necessitates a spatial averaging step at the receive end for remote sensing [48]. This requires a prohibitively large number of receivers to obtain an analogously effective linear reconstruction procedure in the multistatic geometry [49]. When the number of transmitters and receivers is limited, the performance of the linear procedure degrades in imaging extended targets or dense point-target environments [50].

C. Our Approach and Its Advantages

In this article, we use stochastic waveforms in a multistatic SAR configuration to generate a random forward model. Our motivation for this is to utilize the state-of-the-art theory, methods, and algorithms of phase retrieval based on nonconvex optimization for phaseless SAR. In particular, we use the WF framework to solve the quadratic system of equations obtained from the phaseless SAR data model. WF has readily established performance guarantees for Gaussian forward models and certain coded diffraction patterns [51]. However, Gaussianity of the forward map is not a necessary but a sufficient condition for the exact recovery theory of WF. In [40], we have extended the theoretical guarantees of the WF algorithm to arbitrary models. Although our initial motivation in using stochastic waveforms and multistatic configuration is rooted in achieving a Gaussian forward model, our study shows that even with large deviation from Gaussianity, i.e., using a small number of transmitters, the

WF method has the capability of near-exact recovery. Toward maximizing the impact of our work for applicability to different imaging scenarios and conditions, we consider multiple algorithmic modifications to the standard WF method. Namely, we consider different initialization methods for the WF algorithm, using standard spectral initialization and an initialization based on Itakura–Saito divergence minimization [52]. Additionally, we consider the impact of using ℓ_1 regularization in the problem formulation with limited number of measurements and in the presence of noise. The advantages of our approach as compared to the existing methods can be summarized as follows.

1) Unlike the linear reconstruction technique of phaseless RCI [49], our method does not necessitate the idealized assumptions of spatial incoherence or Gaussianity and can reliably reconstruct images of extended targets and dense target environments using a single receiver and a much smaller number of transmitters than that of phaseless RCI.
2) Our method does not require a priori support information to overcome the limitations of the Fourier phase retrieval problem, which arises with monostatic or bistatic SAR configurations with conventional illumination. Furthermore, unlike the work in [25], we do not require full spatial diversity in receive and transmit. In our method, the limitations of Fourier phase retrieval are alleviated using illumination diversity across slow-time and fast-time frequency samples arising through the randomness of the transmitted waveforms.
3) Unlike the work in [6] where sequential pulsing is needed to recover the missing phase, our method solves the quadratic system of equations for phaseless SAR image reconstruction. Therefore, our approach alleviates the need for increased acquisition time per antenna location and provides improved applicability to airborne SAR.

Ultimately, our advantages stem from leveraging the fundamental quadratic nature of the phaseless data model and utilizing the optimization-based approach for phaseless SAR. We demonstrate that even with a very small number of transmitters, WF-based reconstruction is capable of producing near-exact phaseless SAR imaging using a single receiver. Furthermore, we consider the number of transmitters and receivers within the tradeoffs of performance and system costs for phaseless SAR in quantifying the advantages of our method and evaluate the performance of our algorithms with respect to the number of transmitters, receivers, measurement noise, and pulse repetition frequency (PRF). While we are primarily interested in radar imaging applications, our method and algorithms are also applicable to phaseless synthetic aperture imaging using acoustic, ultrasonic, optical, and seismic waves.

D. Organization of This Article

The rest of this article is organized as follows. Section II presents the problem statement for phaseless SAR and the multistatic signal model with stochastic waveforms. Section III presents the WF framework for phaseless SAR and the algorithmic variations for different imaging scenarios. Section IV
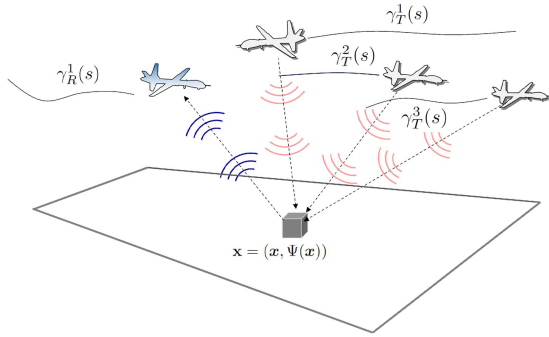
Fig. 1.   Geometry of multistatic SAR.

presents our numerical simulations. Finally, Section V concludes this article.

II. PROBLEM STATEMENT

A. Multistatic SAR Model

Let $\rho : \mathbb{R}^2 \to \mathbb{R}$ denote the ground reflectivity function, and $\Psi : \mathbb{R}^2 \to \mathbb{R}$ be the ground topography function. We let the spatial variable be $\mathbf{x} = (\boldsymbol{x}, \Psi(\boldsymbol{x})) \in \mathbb{R}^3$ representing the surface of the Earth, where $\boldsymbol{x} = (x_1, x_2) \in D \subset \mathbb{R}^2$. We assume an imaging configuration with L number of transmitters simultaneously illuminating a scene of interest, and K number of receivers measuring the magnitude of the back-scattered field, as depicted in Fig. 1. To simplify our description, without loss of generality, we assume a side looking omnidirectional antenna and ignore the geometric spreading factors. Let ω denote the fast-time frequency variable, and $s \in [S_0, S_1]$ denote the slow-time variable. Assuming that the receivers and transmitters traverse the trajectories $\gamma_R^k, \gamma_T^l : \mathbb{R} \to \mathbb{R}^3$, under the start–stop and Born approximations, the backscattered signal at the receiver location can be modeled as follows [53], [54]:

$$f^k(\omega, s) \approx \mathcal{F}^k[\rho](\omega, s) := \int_D \rho(\boldsymbol{x}) F^k(\omega, s, \boldsymbol{x}) d\boldsymbol{x} \quad (1)$$

where $f^k(\omega, s)$ is the backscattered signal at the location of the kth receiver, $k = 1, \dots, K$ at each slow-time $s \in [S_0, S_1]$. In (1), $\omega \in [\omega_c - B/2, \omega_c + B/2]$ where ω_c is the carrier frequency, and B is the bandwidth of the transmitted waveforms. The kernel $F^k(\omega, s, \boldsymbol{x})$ is obtained from the superposition of the L transmissions as follows:

$$F^k(\omega, s, \boldsymbol{x}) = E(\omega, s, \boldsymbol{x}) e^{-i\omega \|\mathbf{x} - \gamma_R^k(s)\|/c_0} \quad (2)$$

where $E(\omega, s, \boldsymbol{x})$ is the incident field at $\boldsymbol{x}$

$$E(\omega, s, \boldsymbol{x}) = \sum_{l=1}^L P_l(\omega, s) e^{-i\omega \|\mathbf{x} - \gamma_T^l(s)\|/c_0} \quad (3)$$

with $P_l(\omega, s)$ denoting the transmitted waveform from the lth transmitter at each slow-time, in the fast-time frequency domain. Hence, $F^k(\omega, s, \boldsymbol{x})$ is equivalent to the scattered field due to a point target at position $\boldsymbol{x}$, and merely the multiplication of the incident field E at location $\boldsymbol{x}$, with Green's function propagator from $\boldsymbol{x}$ to the receiver location at slow-time s. We note that the

geometric spreading factors were ignored in (2) and (3) in line with the far-field and small-scene assumptions.

In phaseless SAR, our objective is to recover the scene reflectivity, ρ, from the intensity-only measurements d^k, for $s \in [S_0, S_1]$ and $\omega \in [\omega_c - B/2, \omega_c + B/2]$, defined as follows:

$$d^k(\omega, s) = |f^k(\omega, s)|^2, \quad \text{for } k = 1, \dots, K \quad (4)$$

where $|\cdot|^2$ denotes the modulus squared.

In conventional SAR, letting t denote the fast-time variable, the transmitted pulse is typically a linear frequency-modulated waveform that is identical for all s as

$$p(t, s) = \exp(-i\pi\alpha t^2)\text{rect}(t/T)e^{-i\omega_c t} \quad (5)$$

where α is the chirp-rate, T denotes the pulse duration, and $\text{rect}(t/T)$ is a windowing function of length T, and ω_c is the carrier frequency. Notably, the chirp signal has an effective bandwidth of αT with $|P(\omega, s)| \approx 1$. However, in conventional monostatic or bistatic SAR with a single transmitter illuminating a chirp signal, the phaseless SAR problem in the far-field reduces to the 2-D Fourier phase retrieval problem. Consequently, the phaseless SAR problem in conventional geometry and waveforms contains certain fundamental ambiguities that are observed in the Fourier phase retrieval problem, in the form of shift-invariance, and reflection-invariance, i.e., the inability to recover the location of a point target from the magnitude of its Fourier transform.

B. Stochastic Waveforms for Phaseless SAR

We assume that each transmitter is emitting the following waveform [49]:

$$p_l(t, s) = C_l(t, s)\exp(i(\omega_l(t, s)t + \phi_l(t, s))) \quad (6)$$

where $\omega_l(t, s), \phi_l(t, s), C_l(t, s)$ are sampled from the uniform distributions as follows:

$$\omega_l(t, s) \sim U[\omega_c - B/2, \omega_c + B/2], \quad \phi_l(t, s) \sim U[-\pi, \pi] \quad (7)$$

and

$$C_l(t, s) \sim U[0, 1], \quad \text{for each } t, s \text{ and } l = 1, \dots, L. \quad (8)$$

The resulting incident field from the superposition of illuminations from L-transmitters approaches to a Gaussian field as $L \to \infty$ via the central limit theorem [41], [49]. The increasing randomness in the spatial patterns of the kernel F^k with increasing L is depicted over a small area in Fig. 2.

Our motivation in adopting these waveforms is the randomness of the kernel F^k, arising due to the stochastic nature of their modulation, and the superposition of the incident fields. While phase retrieval methods were classically studied in the context of optics and Fourier phase retrieval by leveraging prior information and optimization-based methods [55], [56], [57], [58], [59], the past decade has witnessed a resurgence in the theoretical study of the problem using statistical forward models [9], [30], [51], [60], [61], [62], [63], [64], [65]. Existing performance guarantees for state-of-the-art optimization methods in the phase retrieval literature predominantly consider a forward model realized from the i.i.d. Gaussian distribution for establishing exact
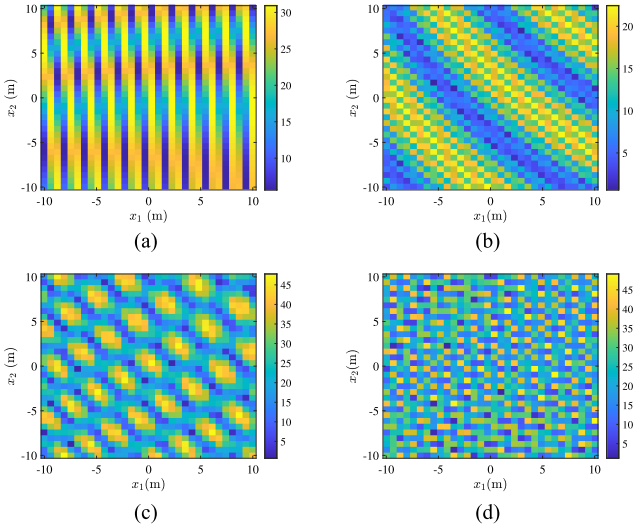
Fig. 2. Sample spatial patterns of the incident field for the superposition of stochastically sampled waveforms as (3) for $L = 2, 3, 4, 5$ transmitters contained with 2000×2000 m^2 area centered at the origin. The incident field intensities are depicted in the temporal-frequency domain, over a 20×20 m^2 area centered at the origin of the coordinate system. The scene is discretized into 32×32 pixels at 0.6-m pixel spacing at the carrier wavelength with $\omega_c = 9.6$ GHz, and $B = 300$ MHz. (a) 2-transmitter illumination. (b) 3-transmitter illumination. (c) 4-transmitter illumination. (d) 5-transmitter illumination.

recovery of the unknown despite the nonconvex nature of the problem [29], [51]. On the other hand, despite their theoretical basis, these works have limited applicability to inverse problems with conventional imaging configurations stemming from the arising deterministic inverse scattering models.

Using the waveforms in (6) ultimately facilitates the realization of random forward models in realistic imaging configurations, thereby addressing the existing gap between the theory and practice of phaseless imaging for remote sensing applications.

C. Motivation for Optimization-Based Phaseless SAR

In using (6), we are inspired by the RCI method in [49], where the following linear reconstruction formula is adopted for phaseless SAR image reconstruction:

$$\hat{\rho}_{F^k}(\boldsymbol{z}) = \int |F^k(\omega, s, \boldsymbol{z})|^2 \left| \int \rho(\mathbf{x}) F^k(\omega, s, \boldsymbol{x}) d\boldsymbol{x} \right|^2 d\omega ds. \tag{9}$$

If F^k is a spatially incoherent, Gaussian field and *ergodic*, then (9) recovers the following estimate of ρ:

$$\hat{\rho}_{F^k}(\mathbf{z}) \approx |\rho(\boldsymbol{z})|^2 + \|\rho\|_2^2 \, \mathbb{E}[|F^k(\boldsymbol{z})|^2] \tag{10}$$

which is the *intensity* of the reflectivity function up to a bias term.

However, for the phaseless RCI method, spatial incoherence, Gaussianity, and ergodicity are *necessary conditions* for the linear reconstruction formula in (9) to produce (10). Due to these requirements, the treatment of phaseless SAR problem within the coincidence imaging framework has certain limitations; including a prohibitively large number of receivers to invoke spatial incoherence, prohibitively large number of transmitters

to invoke Gaussianity, and large number of measurements to invoke ergodicity. On the other hand, our method can recover the scene reflectivity with a limited number of measurements, and a much smaller number of transmitters and receivers by alleviating the necessary conditions and replacing them with sufficient conditions for exact recovery using the established phase retrieval framework of WF [40], [51].

III. PHASELESS SAR VIA NONCONVEX OPTIMIZATION

Optimization-based phase retrieval aims to solve the original *quadratic* inverse problem defined in (1)–(4), using convex or nonconvex methods. To formulate the optimization problem, we start with the discretization of the model in (1).

We discretize the frequency and slow-time variables into a total of M samples $(\omega, s)_{m=1}^M$ and the ground plane into N grid points $\{\boldsymbol{x}_n\}_{n=1}^N$. We define the entries of the discrete measurement map as follows:

$$[\mathbf{L}_m^k]_n = F^k((\omega, s)_m, \boldsymbol{x}_n) \quad n = 1, \cdots N, \; k = 1, \ldots, K. \tag{11}$$

We organize the data at the kth receiver into a vector of size M, defined as $\mathbf{d}^k = [|f_k((\omega, s)_m)|^2]_{m=1}^M$, such that

$$d_m^k := |f_k((\omega, s)_m)|^2 = |\langle \mathbf{L}_m^k, \boldsymbol{\rho}^t \rangle|^2 \tag{12}$$

where $\boldsymbol{\rho}^t \in \mathbb{C}^N$ models the ground truth scene reflectivity function defined as $[\boldsymbol{\rho}^t]_n = \rho(\boldsymbol{x}_n)$.

We then address the phaseless SAR imaging problem by solving the following optimization problem:

$$\hat{\boldsymbol{\rho}} = \underset{\boldsymbol{\rho} \in \mathbb{C}^{\mathbb{N}}}{\operatorname{argmin}} \, \mathcal{J}(\boldsymbol{\rho}) := \frac{1}{KM} \sum_{k=1}^K \sum_{m=1}^M \left| d_m^k - |\langle \mathbf{L}_m^k, \boldsymbol{\rho} \rangle|^2 \right|^2. \tag{13}$$

Despite the ill-posed nature of the problem in (13), there has been a significant progress in the development of provably good algorithms in the last decade. The lifting-based convex optimization methods provide a profound perspective in the study of performance guarantees using low-rank matrix recovery theory [66], [67], [68], [69], [70], [71]. However, the practical drawbacks such as increased computational complexity and memory requirements of these algorithms lead to the study of nonconvex methods that operate on the original signal domain. WF and its variants, thus, provide significant reductions in computational complexity, and memory requirements per iteration, by directly approaching the nonconvex optimization with the factored form of a rank-1, positive semidefinite (PSD) unknown in the equivalent lifted domain [39].

A. WF Algorithm

Using an initial estimate $\boldsymbol{\rho}^0$, the WF algorithm uses gradient descent updates on $\boldsymbol{\rho}$, leading to the following iterations:

$$\boldsymbol{\rho}^{j+1} = \boldsymbol{\rho}^j - \frac{\mu_{j+1}}{\|\boldsymbol{\rho}^0\|^2} \nabla \mathcal{J}(\boldsymbol{\rho}^j) \tag{14}$$

where

$$\nabla \mathcal{J}(\boldsymbol{\rho}^j) = \frac{1}{K} \sum_{k=1}^K \frac{1}{M} \left[\sum_{m=1}^M (\mathbf{e}^{k,j})_m \mathbf{L}_m^k (\mathbf{L}_m^k)^H \right] \boldsymbol{\rho}^j \tag{15}$$

Algorithm 1: ℓ_1-Regularized WF.

Input. $\boldsymbol{\rho}^0$, $\{\mathbf{L}_m^k\}_{m=1,k=1}^{M,K}$, $\{\mathbf{d}^k\}_{k=1}^K$
Set. $\lambda \geq 0$, $\mu > 0$, $\varepsilon > 0$, $j = 0$.
while $\|\nabla\ell(\boldsymbol{\rho}^j)\| > \varepsilon$ **do**
 Step 1. Compute $\nabla\mathcal{J}(\boldsymbol{\rho}^j)$ by (15).
 Step 2. $\tilde{\boldsymbol{\rho}}^{j+1} = \boldsymbol{\rho}^j - \mu\nabla\mathcal{J}(\boldsymbol{\rho}^j)$
 Step 3. $\boldsymbol{\rho}^{j+1} = \max(|\tilde{\boldsymbol{\rho}}^{j+1}| - \lambda\mu, 0) \odot \tilde{\boldsymbol{\rho}}^{j+1}/|\tilde{\boldsymbol{\rho}}^{j+1}|$
 Step 4. $j = j + 1$
end while

---

and $(\mathbf{e}^{k,j})_m = ((\mathbf{L}_m^k)^H \boldsymbol{\rho}^j (\boldsymbol{\rho}^j)^H \mathbf{L}_m^k - d_m^k)$. Beyond the standard setting, WF has also been featured in solving regularized phase retrieval problems. Sparse phase retrieval considers augmenting the loss function in (13) with the ℓ_1 regularization as follows:

$$\hat{\boldsymbol{\rho}}_\lambda = \underset{\boldsymbol{\rho}\in\mathbb{C}^N}{\mathrm{argmin}} \; \mathcal{J}(\boldsymbol{\rho}) + \lambda\|\boldsymbol{\rho}\|_1 \qquad (16)$$

where $\lambda > 0$ is the regularization hyperparameter that is tuned to the desired level of sparsity in the solution. The algorithm iterations in (14) are accordingly augmented with the proximity operator associated with the ℓ_1 regularizer as follows:

$$\mathcal{P}_\alpha(\boldsymbol{\rho}) : = \underset{\mathbf{q}\in\mathbb{C}^N}{\mathrm{argmin}} \; \frac{1}{2}\|\mathbf{q} - \boldsymbol{\rho}\|_2^2 + \alpha\|\mathbf{q}\|_1 \qquad (17)$$

$$= \max(|\boldsymbol{\rho}| - \alpha, 0) \odot \boldsymbol{\rho}/|\boldsymbol{\rho}| \qquad (18)$$

where $\alpha = \mu\lambda$, and max, $\odot$, $\cdot/\cdot$, $|\cdot|$ denote elementwise maximum, multiplication, division, and absolute value operations, respectively. The algorithm steps for the general, ℓ_1 regularized WF procedure is summarized in Algorithm 1. Note that setting $\lambda = 0$ reduces Algorithm 1 to the standard WF algorithm.

Algorithm 1 consists of $\mathcal{O}(MN)$ multiplications for each iteration. Solving for data collected over K receivers then results in $\mathcal{O}(KMN)$ computational complexity per iteration. Note that the sparsity-promoting step does not increase the complexity since it is an elementwise operation. Furthermore, the ℓ_1 regularization provides improved performance with reduced PRF and in the presence of additive noise.

B. Initialization of WF Algorithm

The initial estimate in the WF framework is classically obtained by setting $\boldsymbol{\rho}^0$ as the leading eigenvector of the following matrix estimate of the Kronecker scene, $\boldsymbol{\rho}^t(\boldsymbol{\rho}^t)^H$:

$$\hat{\mathbf{X}}_0 = \frac{1}{KM}\sum_{k=1}^K\sum_{m=1}^M d_m^k \mathbf{L}_m^k(\mathbf{L}_m^k)^H \qquad (19)$$

which yields $\lambda_0\boldsymbol{\rho}^0(\boldsymbol{\rho}^0)^H$ from its rank-1, PSD approximation. This is known in the literature as the *spectral initialization* [72], which has a rich history in data analysis for low-rank reconstructions in matrix completion and graph clustering.

The advantage of the optimization-based nonlinear approach over the linear reconstruction is readily observed from (19), since linear reconstruction is equivalent to preserving only the diagonal elements of the spectral matrix estimate $\hat{\mathbf{X}}_0$. Hence, the

reconstruction under the spatial incoherence assumption on the kernel F^k is equivalent to replacing the rank-1 constraint on the underlying lifted unknown $\boldsymbol{\rho}\boldsymbol{\rho}^H$ with that of a diagonal matrix unknown with entries $|\boldsymbol{\rho}_n|^2$. For general scenes that contain extended targets, the ergodicity assumption breaks down with a single receiver, and ignoring the cross-terms in $\boldsymbol{\rho}\boldsymbol{\rho}^H$ causes significant degradation in the reconstructed images. The nonconvex optimization approach of WF remedies this limitation and directly leverages the rank-1 and PSD structure of the lifted unknown in solving the N-dimensional inverse problem.

C. Exact Recovery Guarantees via WF

Motivations for the classical spectral method are rooted in a probabilistic perspective. By the strong law of large numbers, under the assumption that $\mathbf{L}_m^k \sim \mathcal{N}(0, \frac{1}{2}\mathbf{I}) + i\mathcal{N}(0, \frac{1}{2}\mathbf{I})$ for all $k = 1, \ldots, K$, $m = 1, \ldots, M$, the spectral matrix estimate $\hat{\mathbf{X}}_0$ of the Kronecker scene tends to

$$\mathbb{E}\left[\hat{\mathbf{X}}_0\right] = \|\boldsymbol{\rho}^t\|^2\mathbf{I} + \boldsymbol{\rho}^t(\boldsymbol{\rho}^t)^H \qquad (20)$$

as $KM \to \infty$, which has the true solution $\boldsymbol{\rho}^t$ as its leading eigenvector. Intuitively, if the empirically formed data matrix $\hat{\mathbf{X}}_0$ is concentrated around its expectation, it implies an accurate alignment of its leading eigenvector $\mathbf{v}_0$ to the underlying ground truth as follows:

$$\left\|\hat{\mathbf{X}}_0 - (\|\boldsymbol{\rho}^t\|^2\mathbf{I} + \boldsymbol{\rho}^t(\boldsymbol{\rho}^t)^H)\right\| \leq \delta \; \to \; \frac{|\langle\boldsymbol{\rho}^0, \boldsymbol{\rho}^t\rangle|}{\|\boldsymbol{\rho}^t\|} \geq \varepsilon \quad (21)$$

where δ is a small constant that describes the tightness of the concentration, and by definition

$$\boldsymbol{\rho}^0 = \underset{\|\mathbf{v}\|=1}{\mathrm{argmax}} \; \mathbf{v}^H\hat{\mathbf{X}}_0 \mathbf{v}. \qquad (22)$$

Ultimately, the goal for using a spectral method is to achieve a sufficiently large $\varepsilon > 0$ to land within a basin of attraction by the initial estimate, such that the algorithm converges to the true solution, up to a global phase factor, i.e., any $\boldsymbol{\rho}^t e^{i\theta}$, with $\theta \in [0, 2\pi)$. For i.i.d. Gaussian forward models, it is known that exact recovery is achieved with high probability with $\mathcal{O}(N\log N)$ measurements [51]. For arbitrary measurement models, exact phase retrieval via WF is established in [40] using the standard spectral initialization if $\delta < 0.184$ in (21) for all $\boldsymbol{\rho}^t \in \mathbb{C}^N$. To this end, Yonel and Yazici [40] present a geometric framework that generalizes the analysis of nonconvex optimization methods to handle arbitrary measurement models in the equivalent lifted domain, thereby replacing assumptions based on Gaussianity with sufficient conditions for exact recovery.

D. Design of Spectral Methods for Initialization

The sufficient condition for exact recovery with WF is tied to the spectral initialization quality obtained from (22). Namely, the condition in (21) requires that matching the synthesized phaseless data with the measured phaseless data in the Euclidean-sense yields a high correlation between the spectral estimate and the unknown. However, even with the Gaussian forward model, this condition is not satisfied when the number of measurements becomes limited to $\mathcal{O}(N)$ [40], [64].

Algorithm 2: Spectral Method for Initialization.

Input. $\{\mathbf{L}_m^k\}_{m=1,k=1}^{M,K}$, $\{\mathbf{d}^k\}_{k=1}^K$

Set. $h = \mathbf{I}$ or $h = h_{IS}$ in (23).

Step 1. Compute the matrix estimate as:

$$\hat{\mathbf{X}} = \frac{1}{KM} \sum_{k=1}^K \sum_{m=1}^M [h(\mathbf{d}^k)]_m \mathbf{L}_m^k (\mathbf{L}_m^k)^H \quad (24)$$

Step 2. $\mathbf{v}^0 = \underset{\|\mathbf{v}\|=1}{\arg\max} \ \mathbf{v}^H \hat{\mathbf{X}} \mathbf{v}$

Step 3. $\boldsymbol{\rho}^0 = \left(\sqrt{(\mathbf{v}^0)^H \hat{\mathbf{X}} \mathbf{v}^0} \right) \mathbf{v}^0$

In order to address this limitation and improve the initial estimates using spectral methods, in [52], we developed a framework to design spectral estimators that maximally encode the mismatch information of the phase retrieval problem into a correlation metric with the phaseless data using the Bregman representation property. The framework is then used to derive nonlinear filters on the phaseless data, denoted by $h(\cdot)$, which are optimal in minimizing the choice of a Bregman divergence function on the manifold of positive measures. One such spectral method that has demonstrated strong empirical performance on real-data sets for optical diffraction imaging is the Itakura–Saito divergence minimizing nonlinear filter [52]:

$$[h_{IS}(\mathbf{d}^k)]_m = \frac{1 + \hat{\gamma}^k}{\|\mathbf{L}_m^k\|^2 / (\sum_{m'=1}^M \|\mathbf{L}^k_{m'}\|^2)} - \frac{\|\mathbf{d}^k\|_1}{d_m^k} \quad (23)$$

where $\hat{\gamma}^k$ is an estimate computed from the phaseless data $\mathbf{d}^k$ per each $k = 1, \ldots, K$ and the Bregman representative [73]. The algorithms for spectral methods are provided in Algorithm 2, where setting h to be the identity matrix $\mathbf{I}$ delivers the classical spectral method in (19), and setting h as (23) delivers the Itakura–Saito divergence minimizing spectral method.

We refer to our algorithms using the Itakura–Saito minimization-based initialization as WF-IS, and WF-IS-ℓ_1 when used without and with the ℓ_1 regularization term, respectively. Notably, using the filter in (23) adds computational complexity to the overall procedure because the positive-definiteness of the resulting spectral matrix estimate in (24) is broken when $h = h_{\mathrm{IS}}$. Hence, the power iteration does not yield the spectral estimate directly. However, at the cost of this computation, the Itakura–Saito minimizing method is supported by an optimality result for Gaussian measurement models asymptotically [52]. For imaging scenarios involving a large number of transmitters with relatively short apertures, such as the small UAV-based SAR described in [74], WF-IS provides an alternative to the standard WF method to leverage the increased similarity to a Gaussian forward map.

IV. NUMERICAL SIMULATIONS

In this section, we present numerical simulations to demonstrate the performance of the WF algorithms: nonregularized and ℓ_1 regularized WF with classical spectral initialization, and nonregularized and ℓ_1 regularized WF with Itakura–Saito-based
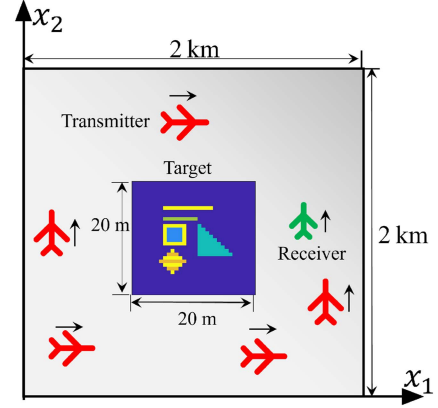

Fig. 3. 2-D schematic of the simulation setup (dimensions not to scale). The transmitters traverse linear trajectories traversing along the x_1 and x_2 axes at different heights. A single receiver traverses along the x_2-axis. The 20×20 m^2 target scene is located at the center of a 2×2 km^2 area.

initialization, henceforth, referred to as WF, WF-ℓ_1, WF-IS, and WF-IS-ℓ_1, respectively. We perform experiments to demonstrate the following:

1) the capabilities of the WF algorithms in reconstructing extended targets;
2) the performance of the WF algorithms with respect to the limited number of transmitters;
3) the advantages of ℓ_1 regularization and IS initialization in different imaging scenarios;
4) the comparison of WF algorithms with the linear algorithm presented in [49];
5) the robustness of the WF algorithms with respect to additive noise.

We use the normalized root-mean-squared error (NRMSE) as a figure of merit to quantitatively evaluate the reconstruction performance. We define the NRMSE as follows:

$$\mathrm{NRMSE} := \frac{\|\boldsymbol{\rho}^t - \hat{\boldsymbol{\rho}}\|_2}{\|\boldsymbol{\rho}^t\|_2} \quad (25)$$

where $\boldsymbol{\rho}^t$ and $\hat{\boldsymbol{\rho}}$ denote the ground truth and the reconstructed images, respectively, and $\| \cdot \|^2$ denotes the ℓ_2 norm.

A. Simulation Setup

Fig. 3 shows the 2-D schematic of the scene with the transmitter and receiver trajectories and the target. We consider a scene of size 20×20 m^2 with flat topography centered at (0,0) m. The scene contains extended objects of different sizes, shapes, and reflectivities. We discretize the scene into 32×32 pixels, which results in a cell size of 0.625×0.625 m^2. Each transmitter emits a total of S pulses, with a pulse duration of 1 μs, and instantaneous frequencies $\omega_l(t)$. The frequencies are sampled from a discrete uniform distribution over [9.5, 9.8] GHz where the uniform distribution is discretized at 15-MHz intervals. The amplitude $C_l(t, s)$ and the phase $\phi(t, s)$ are samples from the distributions $U[0, 1]$ and $U[\pi, -\pi]$, respectively.
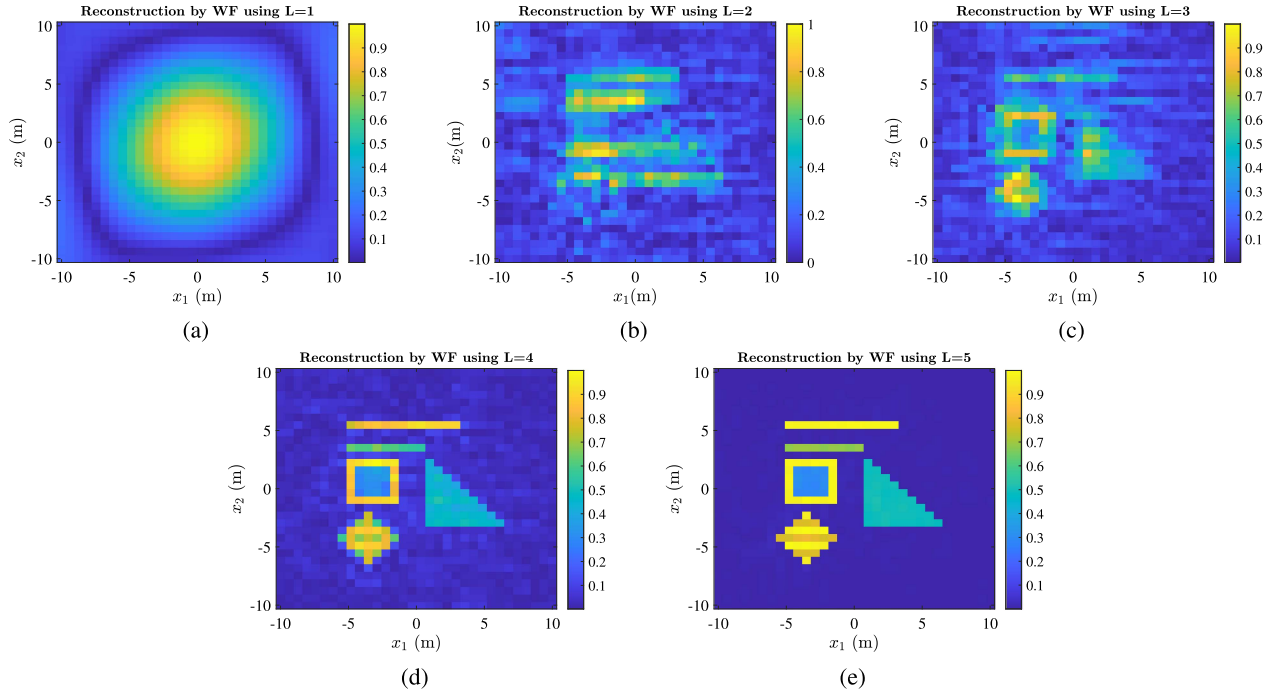
Fig. 4. Reconstructed images by WF using (a) 1, (b) 2, (c) 3, (d) 4, and (e) 5 transmitters. Each transmitter emits 500 pulses over a 1600-m aperture length. Visual inspection of the reconstructed image in (e) shows near-exact recovery.

We assume that the transmitting and receiving antennas are distributed over a 2×2 km^2 area and traverse linear trajectories. Some transmitters traverse along the x_1-axis, and the rest traverse along the x_2-axis at altitudes of 2 km and 1.8 km, respectively. A single receiver travels along the x_2-axis at a height of 1.8 km, as shown in Fig. 3. We choose a speed of travel in the range of 40–60 m/s, suitable for UAV-based SAR systems [75], [76].

B. Performance of the WF Algorithms Using Extended Targets

1) With Respect to Number of Transmitters: In this experiment, we present the reconstructed images of extended targets using a variable number of transmitters ($L = 1, 2, 3, 4, 5$). Each transmitter emits $S = 500$ pulses over a trajectory length of 1600 m. Fig. 4 shows the images reconstructed by the WF algorithm. In each case, all four WF algorithms ran for 1000 iterations. We see that with a single transmitter [see Fig. 4(a)], as expected, WF fails to generate a successful reconstruction, since a single transmitter cannot provide multiple illumination needed. As we increase the number of transmitters, the distribution of F^k approaches to Gaussianity due to the superposition of multiple stochastic waveforms. Although Gaussianity is a sufficient condition for the exact recovery theory of WF, our results show that the WF framework can accommodate large deviations from Gaussianity. We see that the quality of reconstructions improves as the number of transmitters increases [as shown in Fig. 4(b)–(d)] and a near-exact reconstruction is obtained [as shown in Fig. 4(e)] using five transmitters. This observation is further illustrated in Fig. 5, which shows the performance of all four WF algorithms, in terms of NRMSE values, with respect
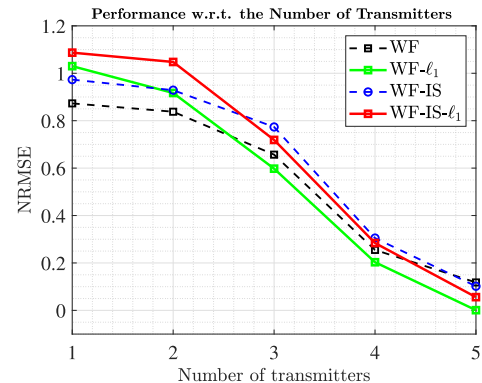

Fig. 5. Average NRMSE with respect to the number of transmitters using a single receiver. Zero NRMSE value at five transmitters shows that WF achieves near-exact reconstructions.

to the number of transmitters. Note that each NRMSE value is obtained by averaging over 10 realizations of the kernel F^k.

2) With Respect to PRF: To demonstrate the effect of ℓ_1 regularization, we consider a scenario where the slow time is sparsely sampled. We consider five transmitters traversing the same trajectory as before (1600 m) and reduce the PRF by a factor of $1/2$, i.e., $S = 250$. Fig. 6(a)–(d) shows the reconstructed images using the WF algorithms. We see that the regularized WF algorithms [see Fig. 6(b) and (d)] reconstruct better quality images than those of their nonregularized counterparts [see Fig. 6(a) and (c)]. In addition, we evaluate the impact of the regularized algorithms in terms of NRMSE values as shown in Fig. 7, for slow-time samples, $S = 50, 100, 250$ (PRF reduced by factors of 1/10, 1/5, and 1/2, respectively). Again, the
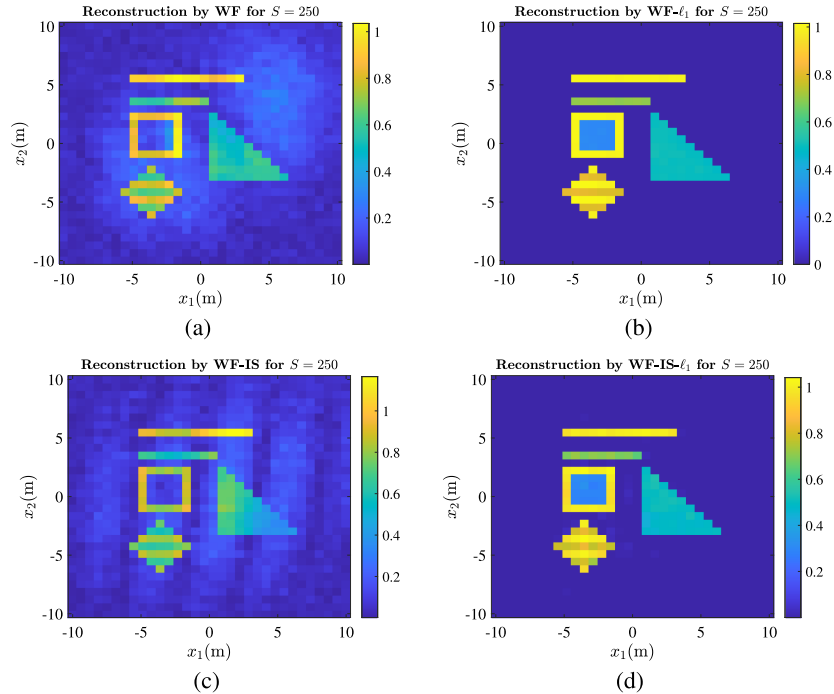
Fig. 6. Reconstructed images by (a) WF, (b) WF-ℓ_1, (c) WF-IS, and (d) WF-IS-ℓ_1 using 250 pulses transmitted from five transmitters.
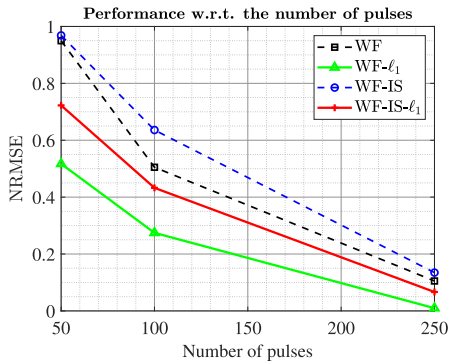

Fig. 7. Average NRMSE w.r.t. the number of slow time samples, $S = 50, 100, 250$ using five transmitters. We see that the regularized WF algorithms provide superior performance for sparsely sampled apertures.

NRMSE values are obtained by averaging over 10 realizations of F^k. It can be clearly seen that for PRF reduction factors of $1/10$ and $1/5$, the regularized WF algorithms perform significantly better than the nonregularized algorithms. We also observe that the WF and WF-ℓ_1 perform better than WF-IS and WF-IS-ℓ_1. This performance can be attributed to the fact that the IS-based initialization is optimal for Gaussian maps, which may require the superposition of pulses from more than five transmitters. Hence, we observe that IS loses its effectiveness compared to the spectral initialization.

C. Reconstruction Performance of WF-IS Compared to WF

We next consider an imaging scenario in which IS-based initialization may provide superior reconstruction performance.

In line with the optimality and measurement efficiency of IS initialization in [52], we consider 10 transmitters with an aperture length of 1600 m uniformly sampled using 50 pulses. Note that in this scenario, the number of slow-time samples is 1/10 of the ones used to reconstruct images shown in Fig. 4, but the number of superpositions (transmitters) is increased by a factor of 2 as compared to the one used in Fig. 4(e). With the increasing number of transmitters, we expect F^k to have a distribution closer to a Gaussian.

Fig. 8 shows the initial images created by the classical spectral initialization and the IS-based initialization. Visual inspection of these images shows that the IS-based initialization provides recognizable structures and a smoother background, producing an image close to the ground truth. Using this initial estimate by IS, we further iterate up to 5000 iterations. Fig. 9(a) and (b) shows the reconstructed images using 5 and 10 transmitters, respectively. Clearly, in this scenario, WF-IS achieves superior performance.

D. Performance of the WF Algorithms for Point Target Reconstructions

In [49], it is shown that with a single receiver, the linear algorithm is not effective in reconstructing extended target scenes even with a prohibitively large number of transmitters. Hence, we compare the performance of the WF algorithms to the linear algorithm using point targets in an imaging configuration close to the one used in [49]. We use $L = 10$ transmitters and a single receiver where each transmitter emits 50 pulses across a 40-m trajectory similar to the setup in [49]. For numerical evaluation, we use the 3-dB main lobe width along the x_1 and x_2 axes of
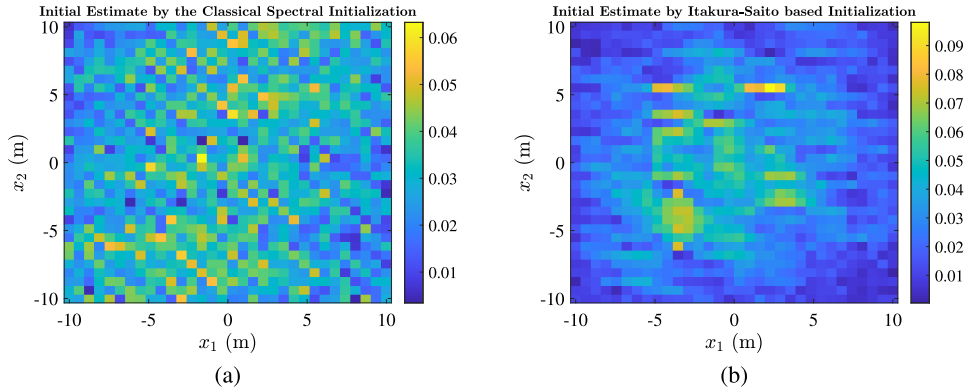
Fig. 8.   Initial estimated images using 10 transmitters transmitting 50 pulses across a 1600-m aperture length, by (a) the classical spectral initialization, and (b) the Itakura–Saito-based initialization.
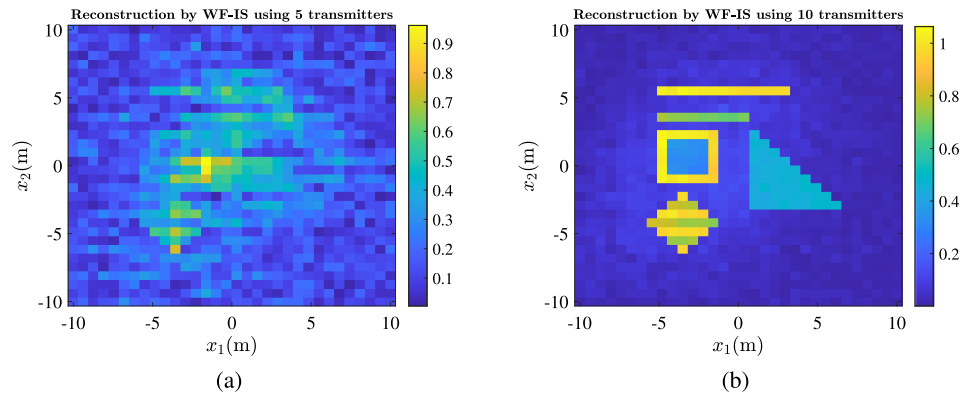

Fig. 9.   Reconstructed images by WF-IS using (a) 5 and (b) 10 transmitters traversing 1600-m trajectory and transmitting 50 pulses.

TABLE I
3-DB MAIN LOBE WIDTH OF THE POINT TARGET RECONSTRUCTIONS

3-dB main lobe width (m)	Linear algorithm	WF	WF-IS	WF-ℓ_1	WF-IS-ℓ_1
x_1 axis	0.7093	0.5653	0.42432	**0.1995**	**0.1479**
x_2 axis	0.7421	0.4629	0.3384	**0.0640**	**0.0581**

TABLE II
CONTRAST [SEE (26)] OF THE LINEAR AND WF ALGORITHMS

Figure of merit	Linear algorithm	WF	WF- IS	WF-ℓ_1	WF-IS-ℓ_1
Mean FBR	17.71	73.49	81.91	78321.54	89404.47

the reconstructed point spread functions (PSFs) as a measure of resolution and the foreground-to-background ratio (FBR) as a measure of contrast. We define the contrast metric as follows:

$$\text{FBR} = \frac{\text{Mean of foreground reflectivity}}{\text{St dev. of background reflectivity}} \qquad (26)$$

where the foreground refers to the true locations of the point targets and the background refers to the rest of the scene. The resolution and contrast values, tabulated in Tables I and II, respectively, are obtained by averaging over 10 realizations of the kernel F^k.

1) Resolution Analysis: In this experiment, we consider a scene with a point target of size 0.625×0.625 m^2, with unit reflectivity, and placed at the (16,16)th pixel. Figs. 10 and 11 show the reconstructed PSFs, along with their profiles along the

x_1 and x_2 axes, by the linear and regularized WF algorithms. We see that the quality of the PSFs improves for the WF algorithms, which is also demonstrated by the lower 3-dB main lobe widths listed in Table I. It can be observed from the table that the regularized WF algorithms (as indicated by the bold values) outperform the nonregularized ones by denoising the backgrounds and suppressing the sidelobes.

2) Contrast Analysis: We place four point targets, with unit reflectivity, of size 0.625×0.625 m^2 at the $(15, 15)$, $(15,17)$, $(17, 15)$, and $(17, 17)$ th pixels, respectively. Fig. 12(a) and (b) shows the images reconstructed by the linear method and WF-IS-ℓ_1, respectively.

Fig. 12 shows that both the linear and WF algorithms reconstruct the point targets at the correct locations. However, the image reconstructed by the linear algorithm has a noisy background and nonuniformity in the foreground. As a result,
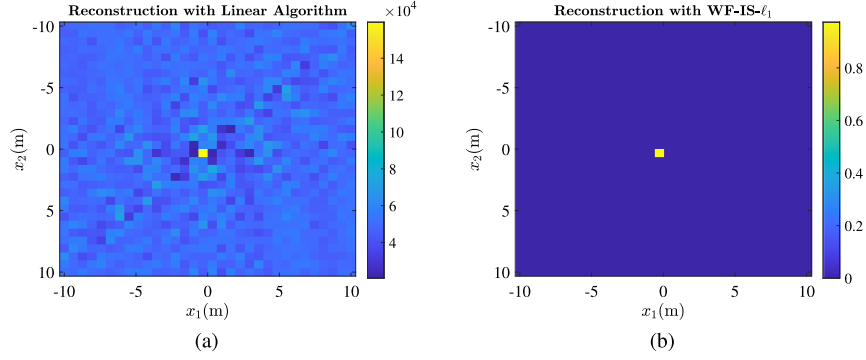
Fig. 10. Reconstructions of a point target using $L = 10$ and a single receiver. (a) Reconstructed image by regularized WF using Itakura–Saito initialization. (b) Reconstructed image by the linear algorithm.
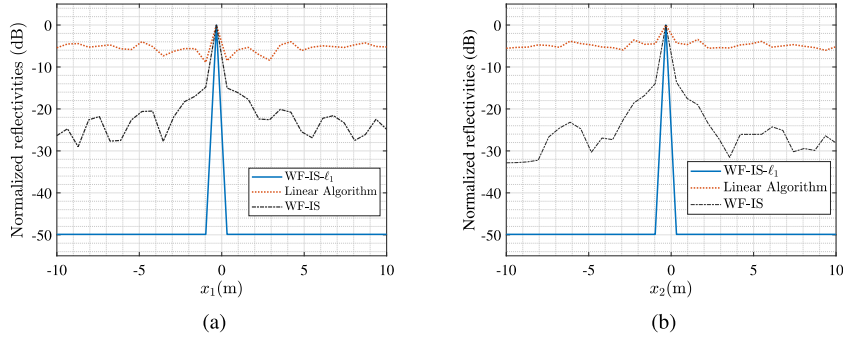

Fig. 11. Reconstructed PSFs along (a) x_1 and (b) x_2 axes of the images shown in Fig. 10.
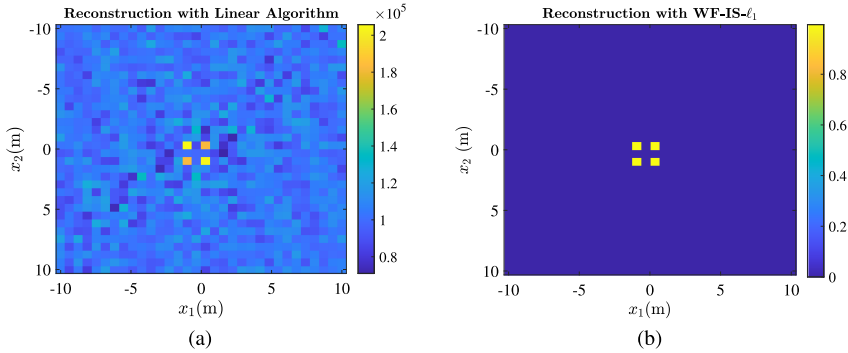

Fig. 12. Reconstructed images of point targets using 10 transmitters and a single receiver. (a) Reconstructed image using the linear algorithm. (b) Reconstructed image using the WF algorithm with Itakura–Saito-based initialization and ℓ_1 regularization.

images reconstructed by the linear algorithm yield low contrast, quantified by FBR tabulated in Table II. Conversely, contrast values improve for the WF algorithms where WF-ℓ_1 and WF-IS-ℓ_1 yield the highest contrast because the WF algorithms produce a relatively uniform foreground and a denoised background due to regularization.

E. Robustness of WF With Respect to Additive Noise

We conduct numerical simulations to evaluate the performance of the WF algorithms (with and without regularization), when the data are contaminated by additive noise. Here, we consider two different noisy data models depending on the origin

of the noise. First, considering the ambient noise, we add zero-mean complex Gaussian noise to the complex back-scattered signal, $f^k(\omega, s)$, and generate the noisy phaseless measurements as follows:

$$d_c^k = \left| f^k(\omega, s) + \epsilon \right|^2 \tag{27}$$

where ϵ denotes the noise vector. We define the signal-to-noise ratio (SNR) as follows:

$$\text{SNR}_c = 10 \log_{10} \left(\frac{\sigma_{f^k}^2}{\sigma_\epsilon^2} \right) \tag{28}$$

where $\sigma_{f^k}^2$ and σ_ϵ^2 denote the variances of the back-scattered data and the noise, respectively. Second, to demonstrate the impact
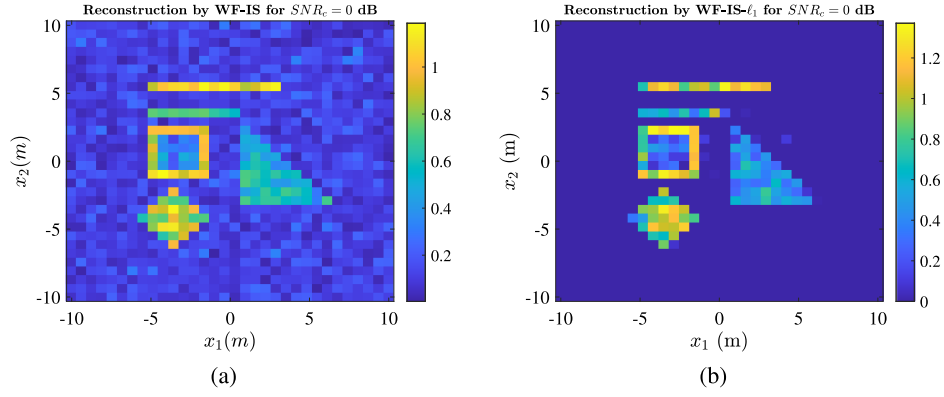
Fig. 13. Reconstructions using the WF-IS algorithm for 0-dB SNR and the data model, $|f^k(\omega, s) + \epsilon|^2$ using (a) no regularization and (b) the ℓ_1 regularization.
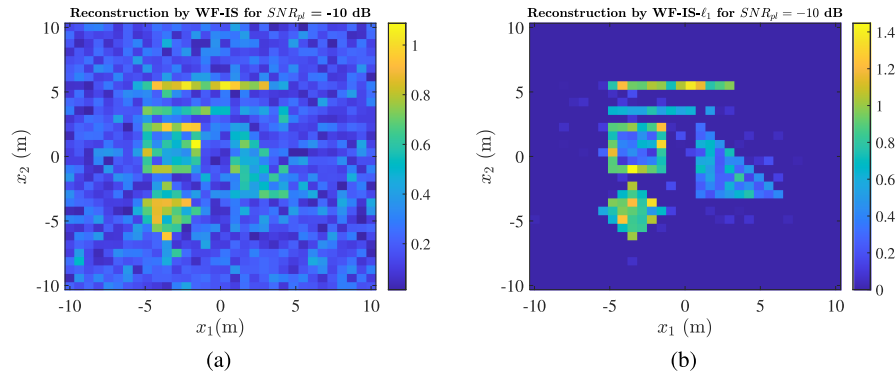

Fig. 14. Reconstructions using the WF-IS algorithm for -10 dB SNR and the noise model, $d^k(\omega, s) + \epsilon_{pl}$ using (a) no regularization and (b) the ℓ_1 regularization.
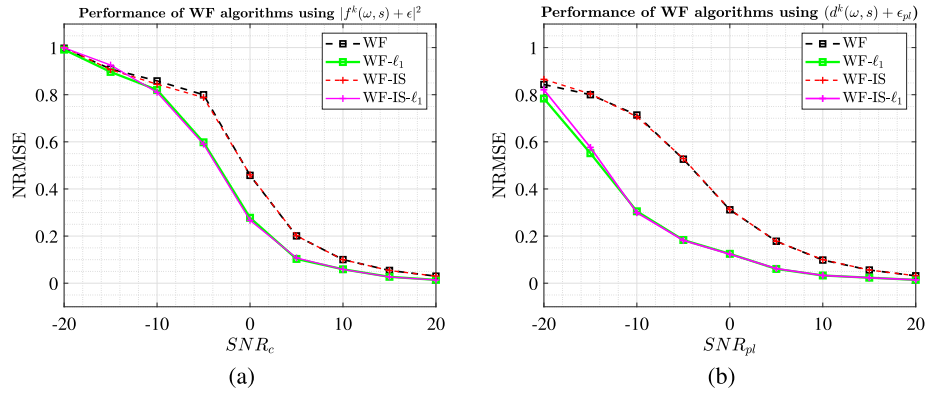

Fig. 15. Performance of the WF algorithms w.r.t. SNR levels using noise models. (a) $|f^k(\omega, s) + \epsilon|^2$. (b) $d^k(\omega, s) + \epsilon_{pl}$.

of electronic noise, we generate the phaseless measurements contaminated with additive real Gaussian noise as follows:

$$y_{pl}(\omega, s) = d^k(\omega, s) + \epsilon_{pl} \qquad (29)$$

where ϵ_{pl} denotes the real-valued Gaussian noise. In this case, we define the SNR as

$$\text{SNR}_{pl} = 10 \log_{10} \left(\frac{\sigma_{d^k}^2}{\sigma_{\epsilon_{pl}}^2} \right) \qquad (30)$$

where $\sigma_{d^k}^2$ and $\sigma_{\epsilon_{pl}}^2$ denote the variances of the phaseless received signal $\mathbf{d}$ and the noise, respectively.

We use the same imaging configuration described in Section IV-A where the scene is illuminated by $L = 5$ transmitters, transmitting $S = 500$ pulses, and a single receiver traversing a 1600-m linear aperture. Using 10 noise realizations for each SNR level, we perform reconstructions using all four WF algorithms. Since the performances of WF and WF-IS are similar, we only show the images reconstructed by WF-IS and WF-IS-ℓ_1 algorithms. Fig. 13 shows the reconstructed images

for the noise model in (27) for 0-dB SNR and Fig. 14 shows the images for the noise model in (29) for -10 dB SNR. In both cases, the ℓ_1 regularization provides improved reconstruction quality by denoising the background.

Finally, we assess the performance of the WF algorithms by demonstrating the NRMSE for different SNR levels. We vary the SNR over the range, $[-20, 20]$ dB, with a step size of 5 dB. For each choice of SNR, we record the average NRMSEs over the 10 realizations of noise. Fig. 15(a) and (b) show the NRMSE versus SNR plots for the noise models in (27) and (29), respectively. For both models, the results demonstrate that whether we use regularization or not, the reconstruction errors monotonically decrease with increasing SNR. The graceful degradation of the image quality with respect to increasing levels of noise shows the robustness of the WF algorithms to additive noise.

V. CONCLUSION

Phaseless SAR is a novel imaging modality offering many advantages including robustness, jamming resistance, reduced hardware complexity, operability in high frequencies, and improved accuracy, and resolution. In this article, we present a novel multistatic phaseless SAR imaging method using stochastic waveforms and nonconvex optimization. Our method generates a random forward map for the multistatic SAR configuration, via the superposition of stochastic waveforms and the spatial diversity of multiple transmitters. The randomness of the forward map is motivated by the state-of-the-art theory, methods, and algorithms in phase retrieval. Specifically, we use the WF framework where the theory shows that under sufficient conditions of the Gaussianity of the forward map, the WF algorithm is guaranteed to recover the true solution. However, our results and the deterministic theory, we developed in [77], show that WF provides superior reconstruction results even if the forward map deviates from Gaussianity significantly, i.e., with a small number of transmitters. We present multiple algorithmic variations on the WF algorithm for different imaging conditions, including ℓ_1 regularization for improved performance with low PRFs and in the presence of additive noise and IS-based initialization for an increased number of transmitters. Our extensive numerical simulations demonstrate significant advantages of our waveform diverse, stochastic transmission scheme coupled with nonconvex-optimization-based reconstruction. We show near-exact recovery with a small number of transmitters and a single receiver under different imaging scenarios for extended targets.

In the future, we will consider optimization of our imaging configuration with respect to different types of transmitted waveforms, and antenna trajectories, and analyze the exact recovery theory for our method under non-Gaussianity assumption. In this work, we employed the standard WF algorithm using ℓ_2-based cost function. However, cost functions, such as reverse Kullback–Leibler divergence [78] can be studied to achieve robustness against outliers and noise. While we are primarily interested in radar imaging applications, our method and algorithms are also applicable to phaseless synthetic aperture imaging using acoustic, ultrasonic, optical, and seismic waves.

REFERENCES

[1] D. Blacknell et al., "Geometric accuracy in airborne SAR images," *IEEE Trans. Aerosp. Electron. Syst.*, vol. 25, no. 2, pp. 241–258, Mar. 1989.

[2] J. Garnier, "Imaging in randomly layered media by cross-correlating noisy signals," *Multiscale Model. Simul.*, vol. 4, no. 2, pp. 610–640, 2005.

[3] T. Isernia, V. Pascazio, R. Pierri, and G. Schirinzi, "Synthetic aperture radar imaging from phase-corrupted data," *Proc. Inst. Elect. Eng.—Radar, Sonar, Navigation*, vol. 143, no. 4, pp. 268–274, 1996.

[4] L. Crocco, M. D'Urso, and T. Isernia, "Inverse scattering from phaseless measurements of the total field on a closed curve," *J. Opt. Soc. Amer. A*, vol. 21, no. 4, pp. 622–631, 2004.

[5] T. Isernia, V. Pascazio, R. Pierri, and G. Schirinzi, "Image reconstruction from Fourier transform magnitude with applications to synthetic aperture radar imaging," *J. Opt. Soc. Amer. A*, vol. 13, no. 5, pp. 922–934, 1996.

[6] M. Moscoso, A. Novikov, G. Papanicolaou, and C. Tsogka, "Synthetic aperture imaging with intensity-only data," *IEEE Trans. Comput. Imag.*, vol. 6, pp. 87–94, May 2019.

[7] M. d'Urso, K. Belkebir, L. Crocco, T. Isernia, and A. Litman, "Phaseless imaging with experimental data: Facts and challenges," *J. Opt. Soc. Amer. A*, vol. 25, no. 1, pp. 271–281, 2008.

[8] W. Zhang, L. Li, and F. Li, "Inverse scattering from phaseless data in the freespace," *Sci. China Ser. F: Inf. Sci.*, vol. 52, no. 8, pp. 1389–1398, 2009.

[9] A. Chai, M. Moscoso, and G. Papanicolaou, "Array imaging using intensity-only measurements," *Inverse Problems*, vol. 27, no. 1, 2010, Art. no. 015005.

[10] A. Novikov, M. Moscoso, and G. Papanicolaou, "Illumination strategies for intensity-only imaging," *SIAM J. Imag. Sci.*, vol. 8, no. 3, pp. 1547–1573, 2015.

[11] J. Laviada, A. Arboleya-Arboleya, Y. Alvarez-Lopez, C. Garcia-Gonzalez, and F. Las-Heras, "Phaseless synthetic aperture radar with efficient sampling for broadband near-field imaging: Theory and validation," *IEEE Trans. Antennas Propag.*, vol. 63, no. 2, pp. 573–584, Feb. 2015.

[12] O. Yurduseven, T. Fromenteze, D. L. Marks, J. N. Gollub, and D. R. Smith, "Frequency-diverse computational microwave phaseless imaging," *IEEE Antennas Wireless Propag. Lett.*, vol. 16, pp. 2808–2811, 2017.

[13] S. D. Blunt et al., "Principles and applications of random FM radar waveform design," *IEEE Aerosp. Electron. Syst. Mag.*, vol. 35, no. 10, pp. 20–28, Oct. 2020.

[14] Z. Ye, D. Zhu, S. Niu, and J. Lv, "Studies on high-resolution airborne synthetic aperture radar image formation with pseudo-random agility of interpulse waveform parameters," *Remote Sens.*, vol. 16, no. 1, 2023, Art. no. 164.

[15] N. H. Lehmann, A. M. Haimovich, R. S. Blum, and L. Cimini, "High resolution capabilities of MIMO radar," in *Proc. 40th Asilomar Conf. Signals, Syst., Comput.*, 2006, pp. 25–30.

[16] T. Derham, S. Doughty, C. Baker, and K. Woodbridge, "Ambiguity functions for spatially coherent and incoherent multistatic radar," *IEEE Trans. Aerosp. Electron. Syst.*, vol. 46, no. 1, pp. 230–245, Jan. 2010.

[17] M. Duarte, M. B. Wakin, D. Baron, and R. G. Baraniuk, "Universal distributed sensing via random projections," in *Proc. 5th Int. Conf. Inf. Process. Sensor Netw.*, 2006, pp. 177–185.

[18] C. R. Berger and J. M. Moura, "Noncoherent compressive sensing with application to distributed radar," in *Proc. 45th Annu. Conf. Inf. Sci. Syst.*, 2011, pp. 1–6.

[19] M. A. Lodhi, H. Mansour, and P. T. Boufounos, "Coherent radar imaging using unsynchronized distributed antennas," in *Proc. IEEE Int. Conf. Acoust., Speech, Signal Process.*, 2019, pp. 4320–4324.

[20] O. Ivanyshyn and R. Kress, "Identification of sound-soft 3D obstacles from phaseless data," *Inverse Problems Imag.*, vol. 4, no. 1, 2010, Art. no. 131.

[21] O. Ivanyshyn and R. Kress, "Inverse scattering for surface impedance from phase-less far field data," *J. Comput. Phys.*, vol. 230, no. 9, pp. 3443–3452, 2011.

[22] M. V. Klibanov, "Phaseless inverse scattering problems in three dimensions," *SIAM J. Appl. Math.*, vol. 74, no. 2, pp. 392–410, 2014.

[23] R. Novikov, "Formulas for phase recovering from phaseless scattering data at fixed frequency," *Bull. Des. Sci. Math.*, vol. 139, no. 8, pp. 923–936, Dec. 2015.

[24] M. V. Klibanov, D.-L. Nguyen, and L. H. Nguyen, "A coefficient inverse problem with a single measurement of phaseless scattering data," *SIAM J. Appl. Math.*, vol. 79, no. 1, pp. 1–27, 2019.

[25] X. Xu, B. Zhang, and H. Zhang, "Uniqueness in inverse scattering problems with phaseless far-field data at a fixed frequency," *SIAM J. Appl. Math.*, vol. 78, no. 3, pp. 1737–1753, 2018.

[26] M. Moscoso, A. Novikov, G. Papanicolaou, and C. Tsogka, "Multifrequency interferometric imaging with intensity-only measurements," *SIAM J. Imag. Sci.*, vol. 10, no. 3, pp. 1005–1032, Jul. 2017.

[27] M. Moscoso, A. Novikov, G. Papanicolaou, and C. Tsogka, "Robust multifrequency imaging with music," *Inverse Problems*, vol. 35, no. 1, 2018, Art. no. 015007.

[28] A. D. Kim and C. Tsogka, "Intensity-only inverse scattering with music," *J. Opt. Soc. Amer. A*, vol. 36, no. 11, pp. 1829–1837, 2019.

[29] J. Sun, Q. Qu, and J. Wright, "A geometric analysis of phase retrieval," *Found. Comput. Math.*, vol. 18, no. 5, pp. 1131–1198, 2018.

[30] A. Fannjiang and T. Strohmer, "The numerics of phase retrieval," *Acta Numerica*, vol. 29, pp. 125–228, 2020.

[31] Y. Shechtman, Y. C. Eldar, O. Cohen, H. N. Chapman, J. Miao, and M. Segev, "Phase retrieval with application to optical imaging: A contemporary overview," *IEEE Signal Process. Mag.*, vol. 32, no. 3, pp. 87–109, May 2015.

[32] K. Jaganathan, Y. C. Eldar, and B. Hassibi, "Phase retrieval: An overview of recent developments," *Opt. Compressive Imag.*, pp. 279–312, 2016.

[33] P. Chen, A. Fannjiang, and G.-R. Liu, "Phase retrieval with one or two diffraction patterns by alternating projections with the null initialization," *J. Fourier Anal. Appl.*, vol. 24, pp. 719–758, 2018.

[34] T. Isernia, G. Leone, and R. Pierri, "Phase retrieval of radiated fields," *Inverse Problems*, vol. 11, no. 1, 1995, Art. no. 183.

[35] F. Soldovieri, A. Liseno, G. D'Elia, and R. Pierri, "Global convergence of phase retrieval by quadratic approach," *IEEE Trans. Antennas Propag.*, vol. 53, no. 10, pp. 3135–3141, Oct. 2005.

[36] B. Yonel, E. Mason, and B. Yazici, "Phaseless passive synthetic aperture radar imaging via Wirtinger flow," in *Proc. 52nd Asilomar Conf. Signals, Syst., Comput.*, 2018, pp. 1623–1627.

[37] E. Mason and B. Yazici, "Robustness of LRMR based passive radar imaging to phase errors," in *Proc. 11th Eur. Conf. Synthetic Aperture Radar*, 2016, pp. 1–4.

[38] R. Moretta and R. Pierri, "Performance of phase retrieval via phaselift and quadratic inversion in circular scanning case," *IEEE Trans. Antennas Propag.*, vol. 67, no. 12, pp. 7528–7537, Dec. 2019.

[39] B. Yonel and B. Yazici, "A generalization of Wirtinger flow for exact interferometric inversion," *SIAM J. Imag. Sci.*, vol. 12, no. 4, pp. 2119–2164, Dec. 2019.

[40] B. Yonel and B. Yazici, "A deterministic theory for exact non-convex phase retrieval," *IEEE Trans. Signal Process.*, vol. 68, pp. 4612–4626, 2020.

[41] D. Li, X. Li, Y. Qin, Y. Cheng, and H. Wang, "Radar coincidence imaging: An instantaneous imaging technique with stochastic signals," *IEEE Trans. Geosci. Remote Sens.*, vol. 52, no. 4, pp. 2261–2277, Apr. 2014.

[42] S. Zhu, A. Zhang, Z. Xu, and X. Dong, "Radar coincidence imaging with random microwave source," *IEEE Antennas Wireless Propag. Lett.*, vol. 14, pp. 1239–1242, 2015.

[43] Y. Cheng, X. Zhou, X. Xu, Y. Qin, and H. Wang, "Radar coincidence imaging with stochastic frequency modulated array," *IEEE J. Sel. Topics Signal Process.*, vol. 11, no. 2, pp. 414–427, Mar. 2017.

[44] X. Wang and Z. Lin, "Microwave surveillance based on ghost imaging and distributed antennas," *IEEE Antennas Wireless Propag. Lett.*, vol. 15, pp. 1831–1834, 2016.

[45] J. H. Shapiro, "Computational ghost imaging," *Phys. Rev. A*, vol. 78, no. 6, 2008, Art. no. 061802.

[46] B. I. Erkmen and J. H. Shapiro, "Ghost imaging: From quantum to classical to computational," *Adv. Opt. Photon.*, vol. 2, no. 4, pp. 405–450, 2010.

[47] J. H. Shapiro and R. W. Boyd, "The physics of ghost imaging," *Quantum Inf. Process.*, vol. 11, no. 4, pp. 949–993, 2012.

[48] B. I. Erkmen, "Computational ghost imaging for remote sensing," *J. Opt. Soc. Amer. A*, vol. 29, no. 5, pp. 782–789, 2012.

[49] A. V. Diebold, M. F. Imani, and D. R. Smith, "Phaseless radar coincidence imaging with a MIMO SAR platform," *Remote Sens.*, vol. 11, no. 5, 2019, Art. no. 533.

[50] E. Mason, I. Y. Son, and B. Yazici, "Passive synthetic aperture radar imaging using low-rank matrix recovery methods," *IEEE J. Sel. Topics Signal Process.*, vol. 9, no. 8, pp. 1570–1582, Dec. 2015.

[51] E. J. Candes, X. Li, and M. Soltanolkotabi, "Phase retrieval via Wirtinger flow: Theory and algorithms," *IEEE Trans. Inf. Theory*, vol. 61, no. 4, pp. 1985–2007, Apr. 2015.

[52] B. Yonel and B. Yazici, "A spectral estimation framework for phase retrieval via Bregman divergence minimization," *SIAM J. Imag. Sci.*, vol. 15, no. 2, pp. 491–520, 2022.

[53] V. Krishnan, J. Swoboda, C. E. Yarman, and B. Yazici, "Multistatic synthetic aperture radar image formation," *IEEE Trans. Image Process.*, vol. 19, no. 5, pp. 1290–1306, May 2010.

[54] L. Wang and B. Yazici, "Bistatic synthetic aperture radar imaging of moving targets using ultra-narrowband continuous waveforms," *SIAM J. Imag. Sci.*, vol. 7, no. 2, pp. 824–866, 2014.

[55] R. W. Gerchberg and W. O. Saxton, "A practical algorithm for the determination of the phase from image and diffraction plane pictures," *Optik*, vol. 35, pp. 237–246, 1972.

[56] J. R. Fienup, "Reconstruction of an object from the modulus of its Fourier transform," *Opt. Lett.*, vol. 3, no. 1, pp. 27–29, Jul. 1978.

[57] R. A. Gonsalves, "Phase retrieval and diversity in adaptive optics," *Opt. Eng.*, vol. 21, no. 5, pp. 829–832, 1982.

[58] H. H. Bauschke, P. L. Combettes, and D. R. Luke, "Phase retrieval, error reduction algorithm, and Fienup variants: A view from convex optimization," *J. Opt. Soc. Amer. A*, vol. 19, no. 7, pp. 1334–1345, 2002.

[59] V. Elser, "Phase retrieval by iterated projections," *J. Opt. Soc. Amer. A*, vol. 20, no. 1, pp. 40–55, 2003.

[60] E. J. Candes, Y. Eldar, T. Strohmer, and V. Voroninski, "Phase retrieval via matrix completion," *SIAM J. Imag. Sci.*, vol. 6, no. 1, pp. 199–225, Feb. 2013.

[61] E. J. Candes and T. Strohmer, "PhaseLift: Exact and stable recovery from magnitude measurements via convex programming," *Commun. Pure Appl. Math.*, vol. 66, no. 8, pp. 1241–1274, Aug. 2013.

[62] I. Waldspurger, A. d'Aspremont, and S. Mallat, "Phase recovery, MaxCut and complex semidefinite programming," *Math. Prog.*, vol. 149, no. 1, pp. 47–81, Feb. 2015.

[63] P. Netrapalli, P. Jain, and S. Sanghavi, "Phase retrieval using alternating minimization," in *Proc. Adv. Neural Inf. Process. Syst*, 2013, pp. 2796–2804.

[64] Y. Chen and E. J. Candés, "Solving random quadratic systems of equations is nearly as easy as solving linear systems," *Commun. Pure Appl. Math.*, vol. 70, no. 5, pp. 822–883, Apr. 2017.

[65] T. Goldstein and C. Studer, "PhaseMax: Convex phase retrieval via basis pursuit," *IEEE Trans. Inf. Theory*, vol. 64, no. 4, pp. 2675–2689, Apr. 2018.

[66] B. Recht, W. Xu, and B. Hassibi, "Necessary and sufficient conditions for success of the nuclear norm heuristic for rank minimization," in *Proc. 47th IEEE Conf. Dec. Control*, 2008, pp. 3065–3070.

[67] B. Recht, W. Xu, and B. Hassibi, "Null space conditions and thresholds for rank minimization," *Math. Prog.*, vol. 127, no. 1, pp. 175–202, Mar. 2011.

[68] S. Oymak, K. Mohan, M. Fazel, and B. Hassibi, "A simplified approach to recovery conditions for low rank matrices," in *Proc. IEEE Int. Symp. Inf. Theory*, 2011, pp. 2318–2322.

[69] B. Recht, M. Fazel, and P. A. Parrilo, "Guaranteed minimum-rank solutions of linear matrix equations via nuclear norm minimization," *SIAM Rev.*, vol. 52, no. 3, pp. 471–501, Aug. 2010.

[70] T. T. Cai, "Sharp RIP bound for sparse signal and low-rank matrix recovery," *Appl. Comput. Harmon. Anal*, vol. 35, no. 1, pp. 74–93, Jul. 2013.

[71] S. Bhojanapalli, B. Neyshabur, and N. Srebro, "Global optimality of local search for low rank matrix recovery," in *Proc. Adv. Neural Inf. Process. Syst*, 2016, pp. 3873–3881.

[72] F. McSherry, *Spectral Methods for Data Analysis*. Seattle, WA, USA: Univ. Washington, 2004.

[73] A. Banerjee, X. Guo, and H. Wang, "On the optimality of conditional expectation as a Bregman predictor," *IEEE Trans. Inf. Theory*, vol. 51, no. 7, pp. 2664–2669, Jul. 2005.

[74] J. Svedin, A. Bernland, A. Gustafsson, E. Claar, and J. Luong, "Small UAV-based SAR system using low-cost radar, position, and attitude sensors with onboard imaging capability," *Int. J. Microw. Wireless Technol.*, vol. 13, no. 6, pp. 602–613, 2021.

[75] Y. Ren, S. Tang, P. Guo, L. Zhang, and H. C. So, "2-D spatially variant motion error compensation for high-resolution airborne SAR based on range-Doppler expansion approach," *IEEE Trans. Geosci. Remote Sens.*, vol. 60, pp. 1–13, Jan. 2021.

[76] V. Koo et al., "A new unmanned aerial vehicle synthetic aperture radar for environmental monitoring," *Prog. Electromagn. Res.*, vol. 122, pp. 245–268, 2012.

[77] B. Yonel, I. Son, and B. Yazici, "Exact multistatic interferometric imaging via generalized Wirtinger flow," *IEEE Trans. Comput. Imag.*, vol. 6, pp. 711–726, Jan. 2020.

[78] N. A. Choudhury, B. Yonel, and B. Yazici, "Robust phase retrieval via reverse kullback-leibler divergence and wirtinger flow," 2024, *arXiv:2204.09791*.

Bariscan Yonel (Member, IEEE) received the B.Sc. degree in electrical engineering from Koc University, Istanbul, Türkiye, in 2015, and the Ph.D. degree in electrical engineering from Rensselaer Polytechnic Institute, Troy, NY, USA, in 2020.

He is currently a Postdoctoral Research Associate with Computational Imaging Group, Rensselaer Polytechnic Institute. His current research focuses on developing theoretical recovery guarantees and efficient algorithmic methods for high-dimensional inference and inverse problems in wave-based imaging. His research interests include applications and performance analysis of machine learning, compressed sensing and optimization methods for inverse problems in imaging, and signal processing.

Nazia Choudhury (Graduate Student Member, IEEE) received the B.Sc. degree in electrical and electronics engineering from the Bangladesh University of Engineering and Technology (BUET), Dhaka, Bangladesh, in 2015. She is currently working toward the Ph.D. degree in electrical engineering with the Computational Imaging Group, Rensselaer Polytechnic Institute, Troy, NY, USA.

Her research interests include optimization methods for inverse problems in imaging and radar.

Birsen Yazici (Fellow, IEEE) received the B.S. degree in electrical engineering and mathematics from Bogazici University, Istanbul, Türkiye, in 1988, and the M.S. and Ph.D. degrees in mathematics and electrical engineering from Purdue University, West Lafayette, IN, USA, in 1990 and 1994, respectively.

From 1994 to 2000, she was a Research Engineer with General Electric Company Global Research Center, Schenectady, NY, USA. From 2001 to June 2003, she was an Assistant Professor with Electrical and Computer Engineering Department, Drexel University, Philadelphia, PA, USA. In 2003, she joined Rensselaer Polytechnic Institute, where she is currently a Full Professor with the Department of Electrical, Computer, and Systems Engineering. She holds 11 U.S. patents. Her research interests include statistical signal processing, machine learning, inverse problems in imaging, and radar.

Dr. Yazici was an Associate Editor for IEEE TRANSACTIONS ON IMAGE PROCESSINGfrom 2008 to 2012, IEEE TRANSACTIONS ON GEOSCIENCES AND REMOTE SENSING from 2014 to 2018, *SIAM Journal on Imaging Science* from 2010 to 2014, and IEEE TRANSACTIONS ON COMPUTATIONAL IMAGING from 2017 to 2020. She was a Distinguished Lecturer of the IEEE Aerospace and Electronics Systems Society from 2020 to 2022 and an elected member of the IEEE Technical Committees on Signal Processing Theory and Methods, Sensor Array and Multichannel, from 2010 to 2020. She is currently an elected member of the IEEE Technical Committees on Computational Imaging.